Characterizing the shape and heat production of open vertical cracks in burst vibrothermography experiments

A. Mendioroz[1], K. Martínez[1,2], R. Celorrio[3], and A. Salazar[1]

[1] Departamento de Física Aplicada I, Escuela de Ingeniería de Bilbao, Universidad del País Vasco UPV/EHU, Plaza Ingeniero Torres Quevedo 1, 48013 Bilbao, Spain.

[2] Instituto Politécnico Nacional (IPN), Centro de Investigación en Ciencia Aplicada y Tecnología Avanzada (CICATA), Unidad Legaria, Legaria 694, Col. Irrigación, C.P. 11500, Ciudad de México, Mexico.

[3] Departamento de Matemática Aplicada, EINA/IUMA, Universidad de Zaragoza, Campus Río Ebro, Edificio Torres Quevedo, 50018 Zaragoza, Spain.

E-mail: arantza.mendioroz@ehu.eus

Abstract

We present a quantitative characterization of the heat flux distribution generated at open vertical cracks in burst vibrothermography experiments. We use a stabilized inversion algorithm that is able to retrieve both homogeneous and inhomogeneous fluxes from surface temperature data generated by open cracks. The performance of the algorithm is checked by inverting both synthetic data with added random noise and experimental data taken on samples containing calibrated heat sources. The results show that it is possible to characterize simultaneously the geometry and the absolute value of the heat flux distribution generated at the crack and therefore, the total emitted thermal power.

Keywords: infrared thermography, vibrothermography, crack characterization, ultrasound excited thermography, inverse problems, nondestructive evaluation, heat source characterization.

1. Introduction

Since the pioneering works in the seventies [1-2], ultrasound excited thermography or vibrothermography (VT) has become an attractive thermographic nondestructive evaluation technique due to its ability to detect defects in a variety of materials: from composite panels [1-8] to massive metallic parts [9-11] as well as in coatings [12]. In this technique, the specimen is excited mechanically, with ultrasounds, and the defects are preferred zones for thermal conversion of the mechanical energy due to different mechanisms. In the case of planar defects, such as cracks, the main mechanism is friction between defect faces [13-16]. In metals, where the ultrasounds damping is low, VT is a defect selective technique since heat is only produced at the defects, whose presence is revealed by a hot spot at the surface, that can be measured by an infrared camera. For an extensive overview of the heat production mechanisms see Ref. [17].

One of the key points for VT to become a fully accepted technique for nondestructive testing is the evaluation of the minimum strain needed to detect a crack and the determination of the minimum detectable crack size. The detectability of cracks in VT experiments is affected by many conditions: it depends on the amount of heat released at the crack, its depth and the thermal properties of the material. The heat released at the crack depends on its size and on the crack closure state and vibration pattern induced in the specimen, which in turn depends on the clamping conditions, the position of the exciter, etc. Due to all these complex interdependences, the research in VT has been focused on several aspects aimed at understanding and improving the detectability of cracks.

In 2009 Morbidini and Cawley proposed a calibration method for VT [18]. They introduced the so-called "heating index" that is a measure of the ability of the vibration field to generate heat at defects. It is estimated from vibration amplitude measurements and takes into account the heat generated at early times, which also contributes to the surface temperature rise. One of the key points is the determination of the minimum strain needed to active a crack in a VT experiment, and to relate the strain level to the energy deposited at a given defect. This requires the evaluation of both the strain coverage, and the thermal power generated at the defect. Holland et al. proposed a method to determine the strain along the sample by scanning the specimen surface with three laser vibrometres in order to get the full 3D vibration field [19]. A much less time consuming method was proposed later on by the same group, using a viscoelastic coating on the metallic part to evaluate the vibration strain distribution from the temperature rise map of the polymer adhesive [20]. The method provides a simple and fast way to obtain full vibration monitoring in a VT test.

Regarding the need to estimate the thermal power deposited at the defect, Holland and Renshaw presented an algorithm that could be used to identify heat sources in a planar specimen from an image sequence [21]. The method consists in using the 2D heat diffusion equation to extract the instantaneous flux distribution from the spatial and temporal derivatives of the image sequence. The authors applied the same processing technique to the case of three dimensional heat propagation, when heat sources are buried below the surface. The resulting "heat source estimate" provides better spatial and temporal resolution than the raw image sequence but the result is not a true heat flux. Another drawback of the method is that the processed image sequence exhibits a reduced sensitivity to deep heat sources if compared to the raw sequence.

In previous works, we tackled the identification of the geometry of buried heat sources from VT experiments, both in modulated [22-26] and burst regimes [27-28]. It is well known that the lock-in technique has the potential to reduce the noise in the data by analyzing a large number of images. This allows detecting very weak signals (far lower than the noise equivalent temperature difference (NETD) of the camera) from defects that would remain unnoticed in a live image sequence, but data taking is rather time consuming. In burst regime, the lowest signal that can be detected is limited by the NETD of the camera, but the experiments are fast, which makes it an ideal technique for industrial applications. The situations that we considered in our previous works were kissing vertical cracks, in which heat is produced all along the crack surface, which leads to the generation of compact heat sources. The geometries we analyzed included rectangles, triangles and semicircles, the latter being representative of kissing half-penny cracks. The identification of the geometry of inner heat sources from surface temperature data, which is a severely ill-posed inverse problem, was carried out by regularizing the least square minimization problem, via the addition of penalty terms.

With the idea of heading for real applications, in this work we focus on burst VT, and we address the characterization of open cracks. Moreover, by inverting raw data corresponding to the absolute temperature increase at the surface we determine not only the geometry, but also the absolute flux distribution and total power generated at vertical cracks. In open cracks the heat generated at the flaw is not characterized by a compact shape, as heat is not produced along all the crack surface. At the center of the crack, where the lips are not in contact, there is no friction so the heat sources have the shape of a band, corresponding to positions where the lips are both in contact and in relative motion. We take the case of semi-circular stripe-shaped heat sources as representative of the behavior of open surface breaking cracks. We check the performance of the inversion algorithm with this type of geometry and its ability to quantify the flux distribution and total power emitted at the crack by inverting synthetic data with added

noise. First, we consider the case in which the flux is homogeneous within the semi-circular band. As a further step to approach experimental situations with real cracks, we also consider inhomogeneous flux production within the band, analyzing three different situations: angle-, depth- and radius-dependent fluxes. Finally, we present inversions of experimental data obtained on samples with calibrated heat sources activated in VT experiments, both homogeneous and inhomogeneous. The results indicate that it is possible to characterize both the heat flux distribution and the thermal power emitted by cracks in VT experiments.

2. Direct and inverse problems

2.1. Direct problem

First, we address the calculation of the evolution of the surface temperature distribution produced by open half-penny vertical cracks, typically encountered in real cracked parts. As mentioned in the introduction, when a constant amplitude ultrasonic burst of duration τ is applied to the cracked specimen, heat is produced at an area that is smaller than the crack, where the lips are in contact and in relative motion, typically featuring the shape of a band [15]. Accordingly, we model the behavior of open cracks in VT experiments as semi-circular band-shaped heat sources.

Figure 1a shows the geometry of a semi-infinite material containing a planar heat source of arbitrary shape Ω in plane Π ($x = 0$), emitting a constant heat flux $Q(\vec{r})$ during a time interval $[0, \tau]$. Under adiabatic conditions at the surface, the general expression for the surface ($z = 0$) temperature evolution is given by [27,28]:

$$T_h(\vec{r}_{z=0},t) = \iint_\Omega \frac{Q(\vec{r}\,')}{2\pi K |\vec{r}_{z=0} - \vec{r}\,'|} Erfc\left[\frac{|\vec{r}_{z=0} - \vec{r}\,'|}{\sqrt{4Dt}}\right] ds' \qquad 0 \le t \le \tau \qquad (1a)$$

$$T_c(\vec{r}_{z=0},t) = \iint_\Omega \frac{Q(\vec{r}\,')}{2\pi K |\vec{r}_{z=0} - \vec{r}\,'|} \left\{ Erfc\left[\frac{|\vec{r}_{z=0} - \vec{r}\,'|}{\sqrt{4Dt}}\right] - Erfc\left[\frac{|\vec{r}_{z=0} - \vec{r}\,'|}{\sqrt{4D(t-\tau)}}\right] \right\} ds' \qquad \tau < t \qquad (1b)$$

Here, K and D are the thermal conductivity and diffusivity of the material, respectively.
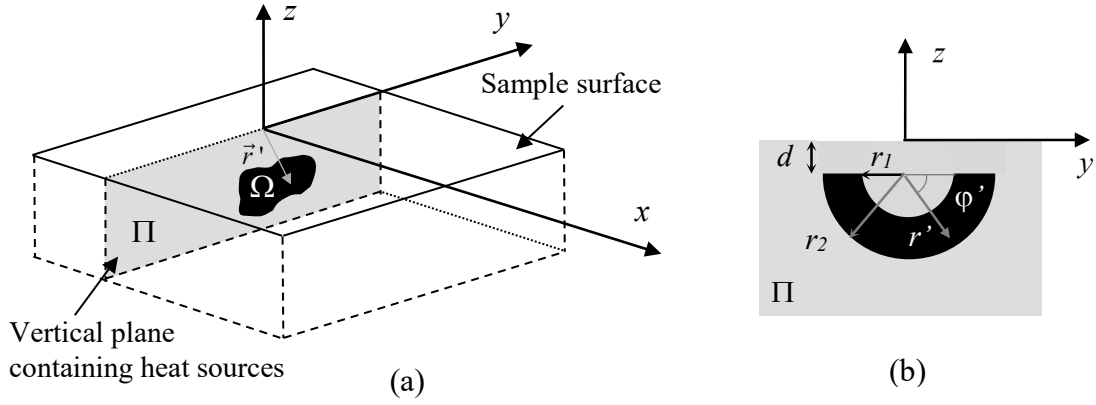
Fig. 1 (a) Geometry of a heat source of area Ω contained in plane Π ($x = 0$). (b) Semi-circular stripe-shaped heat source of inner and outer radii r_1 and r_2, respectively, buried at a depth d.

In the case we address, the particular geometry of the heat source is a semi-circular band of inner and outer radii r_1 and r_2, respectively. For the sake of generality, we consider that the upper side is buried at a depth d below the surface (see Figure 1b). For this geometry, the evolution of the surface temperature distribution during and after the excitation can be expressed as follows:

$$T_h(x,y,0,t) = \int_{r_1}^{r_2} \int_0^\pi \frac{Q(\vec{r}\,')}{2\pi KL} Erfc\left[\frac{L}{\sqrt{4Dt}}\right] r' dr' d\varphi' \qquad\qquad 0 \le t \le \tau \qquad (2a)$$

$$T_c(x,y,0,t) = \int_{r_1}^{r_2} \int_0^\pi \frac{Q(\vec{r}\,')}{2\pi KL} \left\{ Erfc\left[\frac{L}{\sqrt{4Dt}}\right] - Erfc\left[\frac{L}{\sqrt{4D(t-\tau)}}\right] \right\} r' dr' d\varphi' \qquad \tau < t \qquad (2b)$$

where $L = \sqrt{(y - r'\cos\varphi')^2 + (d + r'\sin\varphi')^2}$. Here, r' and φ' are the planar spherical coordinates, with origin at the center of the semi-circles.

The purpose of our work is to invert surface temperature data to determine not only the geometry but also the absolute flux distribution responsible for the observed temperature, in a fast way. In order to reduce the computational cost of the inversion, we extract selected spatial and temporal information: the thermogram obtained at the end of the burst $T_r = T(x,y,0,\tau)$ and the evolution of the temperature at the origin $T_t = T(0,0,0,t)$. Note that T_r and T_t, combined in $T = (T_r, T_t)^T$ (superscript T is transpose), represent absolute values of the temperature elevation at the surface, due to the presence of the crack. Inversion of these raw temperatures will allows us to extract absolute values of the heat flux (and power) emitted by the crack.

2.2. Inverse problem

The inverse problem consists in finding the absolute heat flux distribution ($Q(\vec{r}\,')$ in Eqs. 2a and 2b) responsible for the measured surface temperature. We address the problem without assuming any particular shape of the heat source, only the vertical plane containing the heat sources (easily recognizable from the surface temperature distribution) is taken as prior knowledge. This approach prevents us from addressing the inversion as a parameter estimation problem, in which only the parameters describing a specific geometry are sought. The idea is to mesh the plane that contains the heat sources (plane Π, $x = 0$) and find the heat flux at each node (area element) that minimizes the residual squared R^2, i.e., the square differences between the noisy data, $T^{\delta} = (T_r^{\delta}, T_t^{\delta})^T$, and the calculated temperatures:

$$R^2 := \left\| T_{calc}(Q^{\delta}) - T^{\delta} \right\|^2 \tag{3}$$

where the noise level is defined as $\delta^2 = \left\| T^{\delta} - T \right\|^2$, being $\left\| g \right\|^2 = \iint\limits_{z=0} g^2(x,y)\, dx\, dy$, and Q^{δ} is the retrieved flux distribution from noisy data.

The minimization of R^2 in Eq. (3) involves the determination of a large number of parameters (equal to the number of nodes used to mesh plane Π). Given the diffusive nature of heat propagation, the inverse problem is severely ill-posed and the minimization of the residual in Eq. (3) requires regularization. The stabilization can be carried out by adding regularization terms based on Tikhonov (TK_0) [29], Total Variation (TV) [30], and Lasso (L_1) [31] functionals, defined as:

$$TK_0(Q) = \iint\limits_{\Pi} |Q|^2\, ds \tag{4a}$$

$$TV(Q) = \iint\limits_{\Pi} |\nabla Q|\, ds \tag{4b}$$

$$L_1(Q) = \iint\limits_{\Pi} |Q|\, ds \tag{4c}$$

Based on these penalty terms, the new residual to be minimized writes:

$$R_{\vec{\alpha}^i}^2 = \alpha^i{}_{TK}\, TK_0(Q^{\delta,\vec{\alpha}^i}) + \alpha^i{}_{TV}\, TV(Q^{\delta,\vec{\alpha}^i}) + \alpha^i{}_{L}\, L_1(Q^{\delta,\vec{\alpha}^i}) + \left\| T_{calc}(Q^{\delta,\vec{\alpha}^i}) - T^{\delta} \right\|^2 \tag{5}$$

Here each functional is multiplied by a regularization parameter α that determines the relevance of the stabilizing term with respect to the discrepancy term (last term on the right hand side of Eq (5)). Finding the appropriate values of the regularization parameters is a sensitive issue: they should be high enough to actually stabilize the inversion and, at the same time, as small as possible in order to introduce the smallest error. Our strategy is to start with

rather high values of the regularization parameters and reduce them in successive iterations (for details regarding the inversion algorithm see Ref. [28]). Obviously, the addition of these penalty terms affects the retrieved solution $Q^{\delta,\vec{\alpha}^i}$ (here $\vec{\alpha}^i = (\alpha_{TK}^i, \alpha_{TV}^i, \alpha_{L_1}^i)$ represents the combination of the three regularization parameters). When applying this methodology, the key point is an appropriate determination of the value of $\vec{\alpha}^{i_F}$, when iterations are stopped. For the sake of clarity, in the following we denote the final reconstructed heat flux $Q^{\delta,\vec{\alpha}^{i_F}} = Q_R$. In inversions of synthetic data affected by a given (and accurately known) noise level, applying the Morozov stopping criterion gives excellent results: it consists in stopping iterations when the discrepancy term is of the order of the noise in the data [32]. In inversions of experimental data, on the contrary, the noise level is an uncertain quantity: in addition to the random noise associated to the temperature measurement, data might also be affected by systematic (and unknown) errors. For this reason, the application of the Morozov criterion to experimental data is tricky. In section 4 we will present a new phenomenological criterion to stop the iterations when inverting experimental data.

3. Inversion of synthetic data

In this section we analyze the performance of the algorithm by inverting synthetic data calculated for AISI 304 stainless steel (K = 16 W/mK, D = 4 mm^2/s), which is the material our samples are made of. First, we analyze the case of semi-circular, stripe-shaped heat sources emitting a homogeneous flux. Eqs. (2a) and (2b) have been computed to generate surface temperature data for a semicircular band of inner and outer radii r_1 = 1 mm and r_2 = 2 mm, respectively, buried at a depth d = 0.1 mm and emitting a homogeneous flux of $Q = 5 \times 10^4$ W/m^2, which corresponds to a total emitted power of P_E = 0.234 W. Its 3D geometry is given in Fig. 2a. The effect of changing the radii, the burst duration and the noise level in the data will be analyzed in the following.
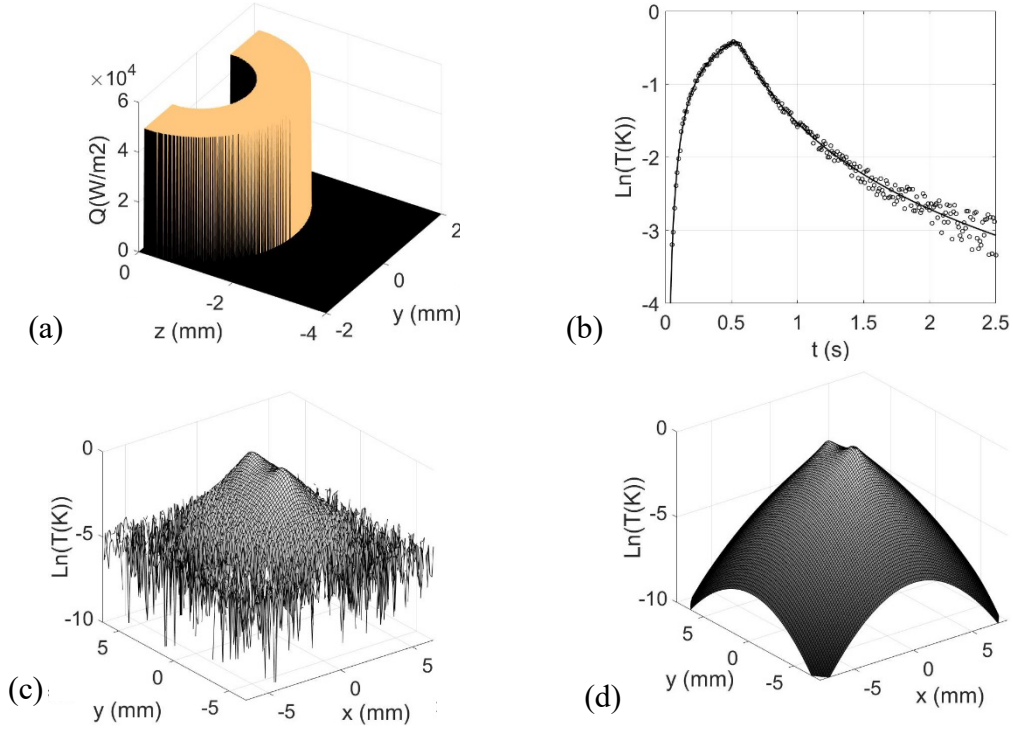
Fig. 2 (a) 3D representation of a semi-circular stripe-shaped heat source of inner and outer radii $r_1 = 1$ mm and $r_2 = 2$ mm, respectively, buried at a depth $d = 0.1$ mm and emitting a homogeneous flux $Q = 5 \times 10^4$ W/m^2. (b) Noisy (5%, symbols) and fitted (solid line) T_t at the central pixel. (c) and (d) Noisy (5%) and (b) fitted T_r, obtained at the end of a $\tau = 0.5$ s.

3.1. Effect of burst duration

We have tested three burst durations: $\tau = 0.5$, 3 and 8 s. In all cases, a 5% random noise, which is similar to that found in VT experiments, have been added. Fig. 2b shows the noisy and fitted temperature evolution at the central pixel, T_t, (symbols and solid line, respectively) corresponding to a burst duration of $\tau = 0.5$ s. Figs. 2c and 2d show the noisy and fitted thermograms T_r calculated at the end of the burst, respectively, for the same burst duration.
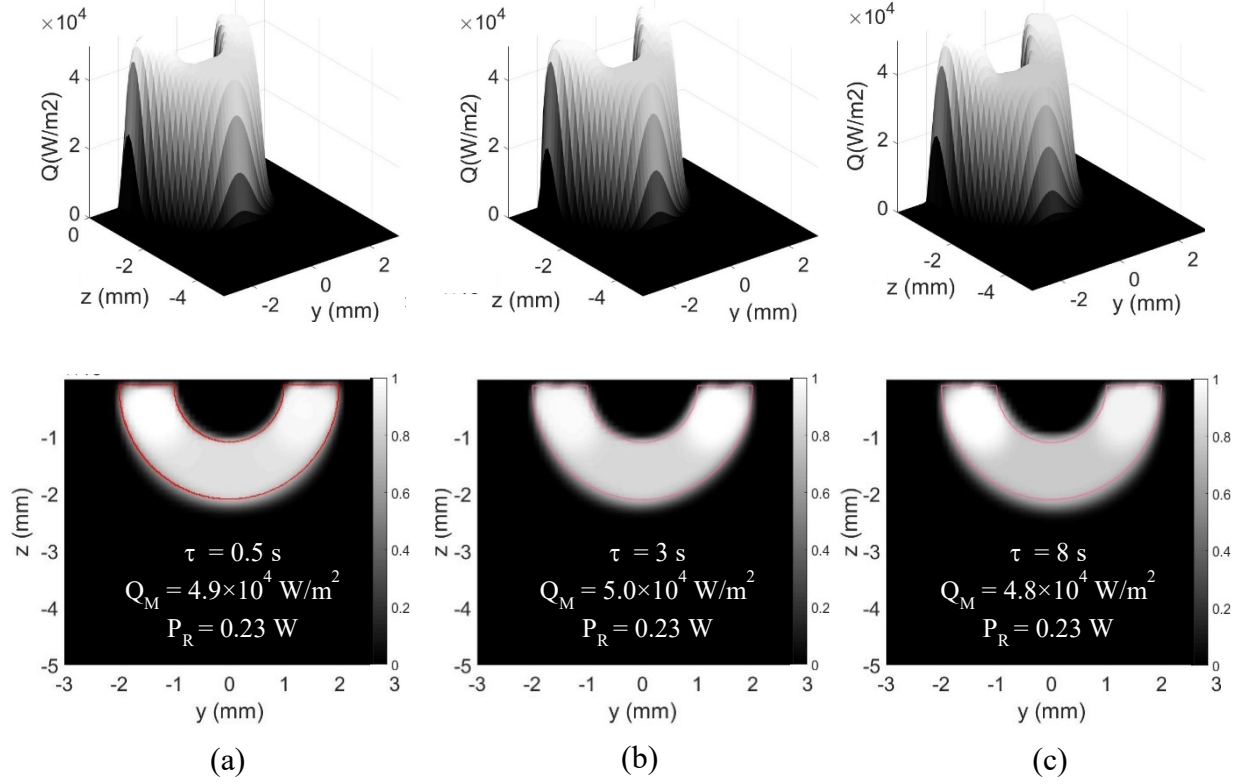
Fig. 3 Top: 3D representation of the retrieved absolute heat flux distribution, $Q_R(\vec{r})$, corresponding to the real heat source depicted in Fig. 2d ($r_1 = 1$ mm, $r_2 = 2$ mm, $d = 0.1$ mm, $Q = 5 \times 10^4$ W/m^2, $P_E = 0.234$ W), obtained from synthetic data corresponding to burst durations of (a) $\tau = 0.5$ s, (b) $\tau = 3$ s, and (c) $\tau = 8$ s, and data affected by 5% noise. Bottom: 2D gray level representation of the normalized heat source distributions, $Q_N(\vec{r})$. The red lines represent the real contours of the heat sources. The retrieved maximum flux Q_M and total power P_R are displayed on each reconstruction.

The reconstructions for the three burst durations are depicted in Figure 3. On top, we present 3D images of the retrieved absolute heat flux distributions, $Q_R(\vec{r})$. In order to better visualize the geometry of the heat sources, at the bottom we display a 2D grey level representations of the normalized heat flux distribution $Q_N(\vec{r})$, which is defined as

$$Q_N(\vec{r}) = \frac{Q_R(\vec{r})}{Q_M}$$, where Q_M is the maximum value of the retrieved heat flux. White represents

$Q_N(\vec{r}) = 1$ and black $Q_N(\vec{r}) = 0$. The values of Q_M and the total retrieved power, P_R, are also specified for each reconstruction. The latter is calculated by adding the values of the flux $Q_R(\vec{r})$ retrieved at each node of the rectangular mesh in plane Π, multiplied by elementary area of the mesh $dx \cdot dy$. As can be observed, not only the geometry of the heat sources is well identified,

9

but also the absolute values of the flux and emitted power are retrieved very accurately. Note that the quality of the reconstructions is rather independent of the duration of the burst.

However, if we reduce the thickness of the stripe down to 400 µm ($r_1 = 1$ mm, $r_2 = 1.4$ mm, $d = 0.1$ mm) while keeping the heat flux $Q = 5 \times 10^4$ W/m^2 (i.e. $P_E = 0.075$ W) and the 5% noise level in the data, the influence of the burst duration on the quality of the reconstruction is more noticeable. As can be observed in Figure 4, a short ($\tau = 0.5$ s) burst that carries a relatively larger high frequency content provides better definition of narrow features than a long burst ($\tau = 5$ s). The reconstructions from long bursts exhibit a shadowing effect: the shallow tips appear brighter and sharper than the deep central side. However, the total retrieved power is rather accurate, the fainter local flux at the deepest side being compensated by the reconstruction overflowing the real contour.
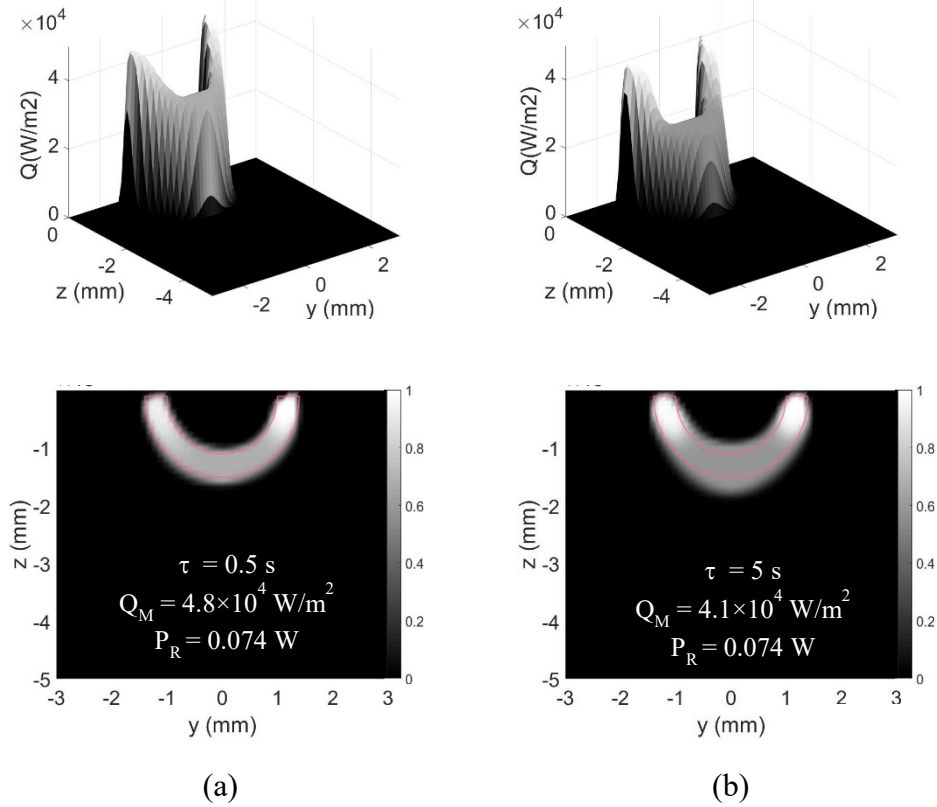

(a)   (b)

Fig. 4 The same as in Fig. 3 but for a narrower heat source of radii $r_1 = 1$ mm and $r_2 = 1.4$ mm, buried at the same depth $d = 0.1$ mm, and emitting the same homogeneous flux of $Q = 5 \times 10^4$ W/m^2 (i.e. $P_E = 0.075$ W). Reconstructions obtained for: (a) $\tau = 0.5$ s and (b) $\tau = 5$ s.

3.2. Effects of noise level and depth

We have also checked the influence of the noise level in the data on the retrieved heat fluxes. In Figure 5 we present reconstructions corresponding to the same heat source depicted in Fig. 2a ($r_1 = 1$ mm, $r_2 = 2$ mm, $d = 0.1$ mm, $Q = 5 \times 10^4$ W/m^2, $P_E = 0.234$ W) obtained from synthetic data calculated for a burst duration of $\tau = 2$ s, affected by three noise levels: 0.5, 5 and 10%.
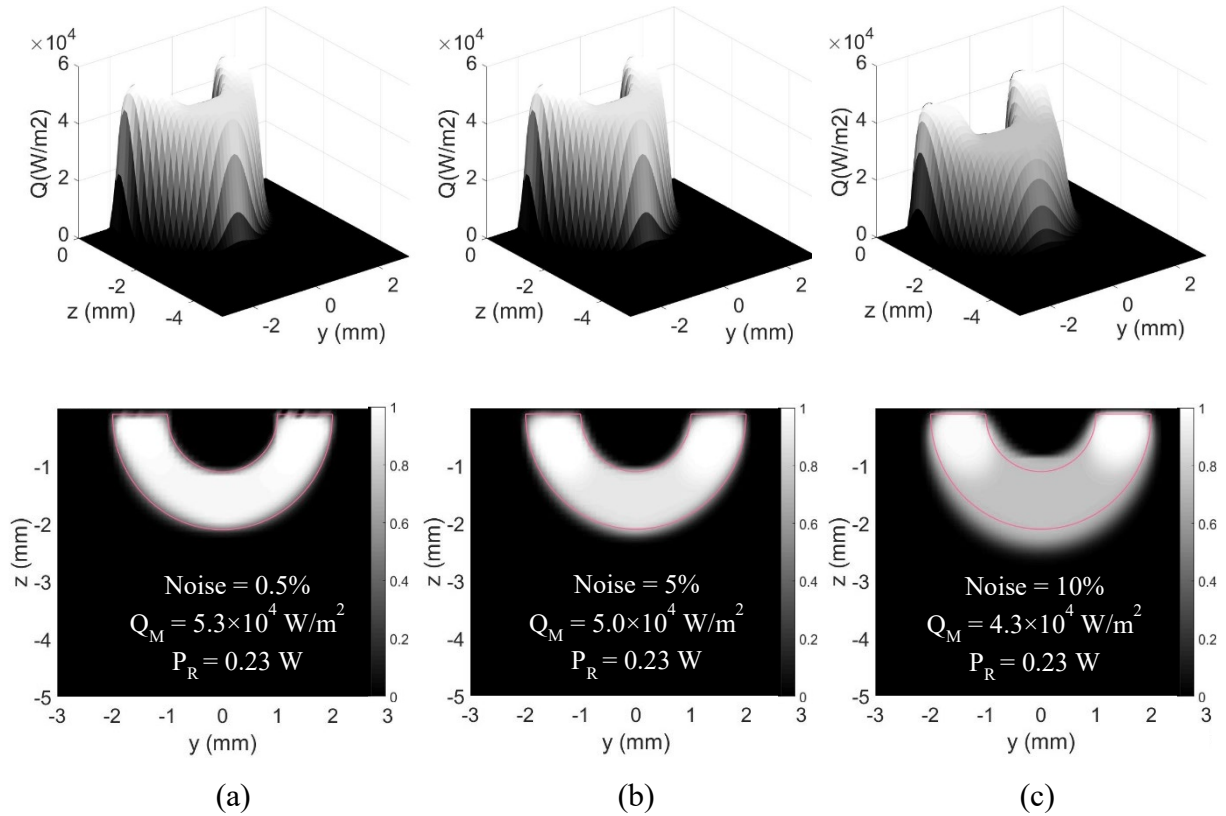

Fig. 5 The same heat source as in Fig. 3, but for a burst duration of $\tau = 2$ s. Three noise levels are considered: (a) 0.5 % and (b) 5% and (c) 10%.

The results in Fig. 5 demonstrate that the noise level in the data affects both the distribution of the flux and the maximum flux value: the larger the noise level, the more pronounced the shadowing effect, meaning that the retrieved heat sources spread over an area larger than the real area they occupy. However, the shadowing effect does not affect the retrieved total emitted power, which is identified very accurately even for data affected by 10% noise.

In the previous examples, we considered typical open surface breaking cracks with heat production reaching the sample surface. For the sake of completeness, we have also considered buried heat sources with the shape of semicircular stripes and we have analyzed the influence

of the depth of heat sources having the same geometry and flux as in Figure 2a ($r_1 = 1$ mm, $r_2 = 2$ mm, $Q = 5 \times 10^4$ W/m^2, $P_E = 0.234$ W), but buried at depths of $d = 0.5$, 1, and 2 mm. The results, corresponding to a $\tau = 2$ second burst and 5% noise in the data, are depicted in Figure 6.
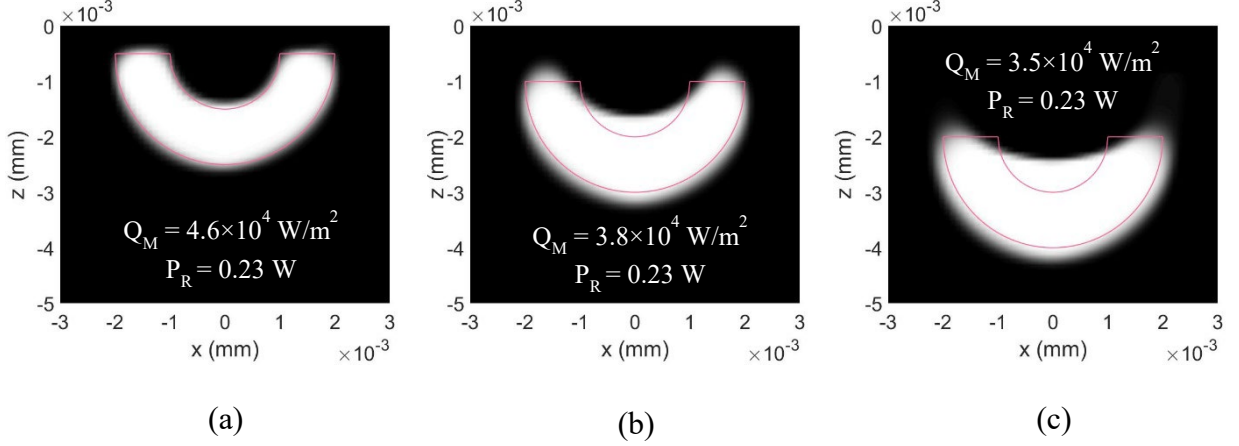

(a)   (b)   (c)

Fig. 6 2D gray level representation of the normalized heat source distributions, $Q_N(\vec{r})$ corresponding to real heat sources of radii $r_1 = 1$ mm and $r_2 = 2$ mm, emitting a homogeneous flux of $Q = 5 \times 10^4$ W/m^2 (total power $P_E = 0.234$ W), and buried different depths (a) $d = 0.5$, (b) $d = 1$ and (c) $d = 2$ mm. Synthetic data calculated for a $\tau = 2$ s burst and affected by 5% noise. The red lines represent the real contours of the heat sources. The retrieved maximum flux Q_M and total power P_R are displayed on each reconstruction.

The results indicate that even if we keep the same noise level at different depths, the quality of the reconstruction decreases: it is harder to reproduce the space in the middle, and the reconstruction overflow the real contour. Besides, once again this comes with a reduction of the maximum retrieved power that compensates for the excess area of the reconstruction, providing a very good estimate of the total emitted power.

3.3. Non-homogeneous heat sources

The results displayed in Figures 3 to 6 correspond to homogeneous heat sources. However, in experiments with real cracked samples, the heat distributions generated at cracks are very likely inhomogeneous. In order to mimic the conditions we have tried to implement in experiments with calibrated inhomogeneous heat sources, we next consider the case of semi-circular stripe-shaped heat sources ($r_1 = 1$ mm and $r_2 = 2$ mm, $d = 0.1$ mm) divided vertically into two equal quarters, each one emitting a homogeneous (but different) flux. We present three cases in which the heat flux emitted by the left quarter (A) remains fixed $Q_A = 5 \times 10^4$ W/m^2

while the right quarter (B) emission varies: $Q_B = 1.25 \times 10^4$, 2.5×10^4 and 3.75×10^4 W/m^2. In Figure 7 we present the 2D grey level representations of the normalized heat flux distributions obtained from synthetic data calculated for a $\tau = 1$ s burst, affected by 5% noise. As can be seen, the reconstructions give good geometrical representations of the two homogeneous quarters, as well as very accurate values of the absolute fluxes and powers in all cases. This result indicates the adequacy of the penalty terms selected to stabilize the inversion.
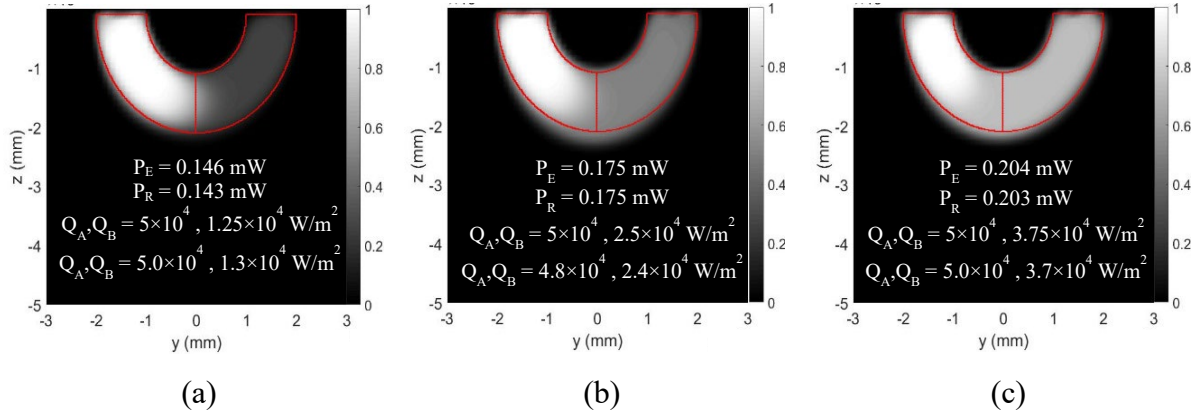

(a)   (b)   (c)

Fig. 7 2D grey level reconstructions obtained for semi-circular stripe-shaped heat sources ($r_1 = 1$ mm and $r_2 = 2$ mm, $d = 0.1$ mm) divided into two quarters. The heat flux on the left is fixed $Q_A = 5 \times 10^4$ W/m^2 while heat fluxes on the right vary: (a) $Q_B = 1.25 \times 10^4$ W/m^2, (b) $Q_B = 2.5 \times 10^4$ W/m^2 and (c) $Q_B = 3.75 \times 10^4$ W/m^2. The third row corresponds to the nominal heat fluxes, while the fourth one stands for the retrieved fluxes at the homogeneous zones of the reconstructions.

In order to further approach real situations in VT experiments with open cracks, in the following we consider three different continuously varying fluxes within semi-circular stripe-shaped heat sources of radii $r_1 = 1$ mm, $r_2 = 2$ mm and depth $d = 0.1$ mm, namely, depth-, angle- and radius-varying fluxes. The 2D grey level representations of the normalized reconstructions are displayed in Figure 8. In all cases, the temperature data for the inversions were calculated for $\tau = 1$ s and for fluxes varying linearly from 0 to 5×10^4 W/m^2 as a function of the corresponding spatial coordinate (lower figures). For each distribution, we display reconstructions obtained by inverting data with two noise levels: 1% and 5%. The nominal and retrieved maximum flux and total power are summarized in Table 1.
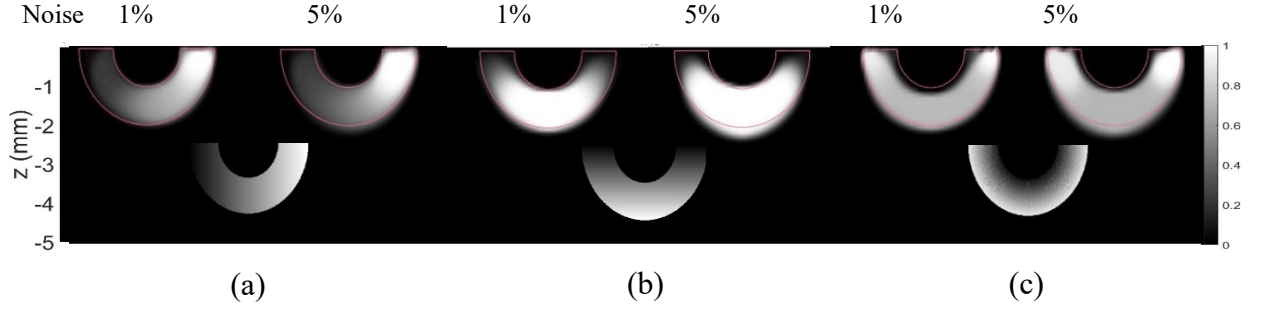
Fig. 8 2D grey level representation of the normalized heat flux distribution, $Q_N(\vec{r})$, corresponding to heat sources of the same shape ($r_1 = 1$ mm and $r_2 = 2$ mm and $d = 0.1$ mm) emitting linear (a) angle-dependent, (b) depth-dependent, and (c) radius-dependent fluxes, obtained from synthetic data corresponding to a burst duration of $\tau = 1$ s and noise levels of 1 % and 5%. The last raw corresponds to the real heat flux distribution.

Inspection of Fig. 8 shows that, although the radius dependent flux is hard to characterize, the geometrical variation of the depth-dependent flux is in qualitative good agreement with the true flux and that the identification of the angle-dependent flux is really accurate. This indicates that the algorithm is able to identify smooth flux variation as opposed to large gradients, the performance being better if the variation is quasi-parallel to the surface, rather than in depth.

On the other hand, the results also show that the quality of the reconstructions depends largely on the noise in the data so, in order to precisely identify inhomogeneous fluxes, a low noise level in the data is highly desirable. Regarding the absolute values of the retrieved fluxes, the coincidence with the nominal values is not that accurate, but once again, the coincidence between the nominal and retrieved total power is excellent.

These results point out to an outstanding ability of the proposed method to identify the thermal power emitted by a vertical crack in VT experiments. Moreover, the geometry of the heat flux and the absolute values of the heat flux distribution can be determined very accurately for blocky-type flux distributions. The method reaches its limits when it comes to identify large continuously varying flux gradients, but the reconstructions of smooth flux variations are noticeably accurate.

Table 1. Nominal and retrieved values of the maximum flux and power corresponding to the reconstructions depicted in Figure 8.

	Angle dependence		Depth dependence		Radius dependence	
Noise level (%)	1	5	1	5	1	5
Nominal Q_M (W/m^2)	5×10^4		5×10^4		5×10^4	
Retrieved Q_M (W/m^2)	4.7×10^4	4.4×10^4	3.0×10^4	2.5×10^4	3.7×10^4	3.2×10^4
Nominal P_E (W)	0.120		0.104		0.130	
Retrieved P_R (W)	0.118	0.118	0.102	0.103	0.128	0.129

4. Experiments and inversion of experimental data

In order to test the method with experimental data, we need to prepare samples that generate calibrated inner heat sources when excited with ultrasounds. The preparation of the samples is intended to produce a homogeneous heat flux. They basically consist of two identical parts, made of AISI 304 stainless steel, featuring perfectly matching, well rectified flat surfaces. A diagram of the samples is depicted in Fig. 9a. We put a Cu slab, 37 μm thick, of known dimensions between the two flat surfaces, and we attach the two parts with screws. When we launch the ultrasounds there is friction between the Cu slab and the steel surfaces, so the Cu slab becomes a heat source. We also place two more Cu slabs of the same thickness at the back side of the flat surfaces, to guarantee that they are parallel. These additional Cu slabs are located far enough from the surface where data are taken, so that they do not disturb the surface temperature distribution generated by the calibrated slab. The parallelism of the two steel parts guarantees a homogeneous heat flux along the surface of the Cu slab.
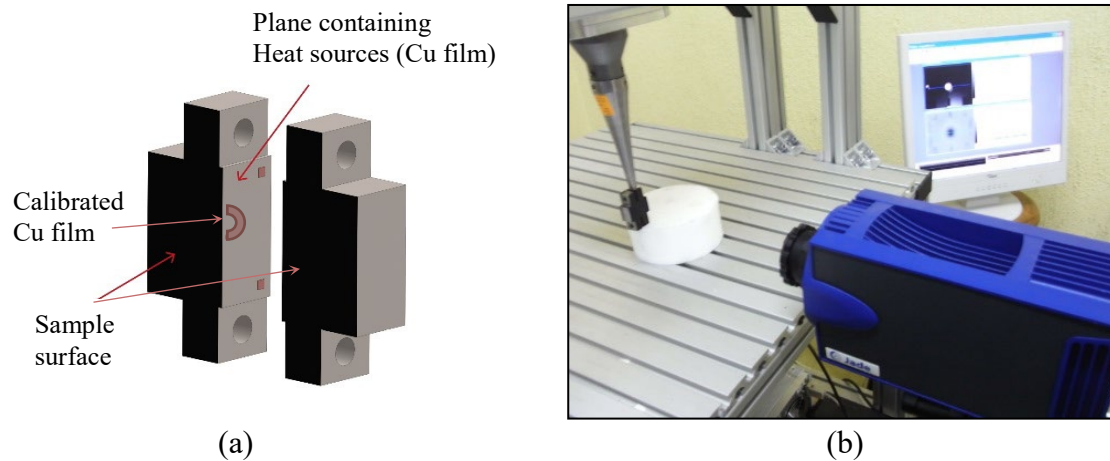
Fig. 9 (a) Diagram of the samples containing the Cu films that act as heat sources when excited by ultrasounds. (b) Picture of the setup with the sample in place for excitation.

The vibrothermography setup is shown in Fig. 9b. We use a tunable (15-25 kHz) ultrasound equipment from Edevis with a maximum power of 2 kW (at 20 kHz), and we excite the sample at a single ultrasound frequency of 22.9 kHz. The sample is excited with constant power bursts ranging from 0.5 to 3.5 s, and ultrasound electrical powers ranging between 60 and 120 W. The sample surface is covered with high emissivity paint. A thin aluminum film is inserted between the sample and the sonotrode to favor the injection of the ultrasounds in the sample. We capture the radiation coming from the sample surface with an infrared video camera (JADE, J550M from Cedip), working in the 3.5 to 5 μm range, equipped with a 320 x 240 detector and a 50 mm focal length lens. We work at the minimum possible distance, for which the spatial resolution is 135 μm. The distance between the camera and sample, room temperature, sample emissivity are fed into the software controlling the camera to get calibrated temperature data. In each film, the first frame is subtracted to obtain the temperature rise above the ambient and to compensate for eventual emissivity inhomogeneities.

We took data on samples containing calibrated Cu slabs of different geometries and dimensions, on which we applied bursts of different durations. As an example, in Fig. 10 we show experimental T_r and T_t data together with the fittings, the residuals, and the evolution of the maximum heat flux distribution Q_M retrieved along the iteration process, for a semi-circular Cu band of radii $r_1 = 1.2$ mm, $r_2 = 2.1$ mm buried at a depth of $d = 0.15$ mm, excited with a burst duration of $\tau = 0.5$ s. As mentioned in section 2, in order to apply the Morozov stopping criterion (which is based on knowledge of the noise in the data) to experimental data,

16

an accurate determination of the noise level in the data is necessary. This is not easy to accomplish with experimental data. Accordingly, we have sought an alternative, phenomenological stopping criterion. We have looked at the maximum retrieved flux along the iteration process Q_M and we have found that the evolution of this quantity features a disruption at the iteration that provides the optimum reconstruction (see Fig. 10f). After this iteration, the maximum flux increases at a rate much larger than the rate in previous iterations, and the area of the reconstructed flux shrinks very fast and features spikes. This is indicative of the minimization becoming unstable due to very low values of the regularization parameters in Eq. 5. The fitings depicted in Fig. 10 have been obtained by stopping the iteration process at iteration no. 21. This stopping criterion has been applied in all the following experimental reconstructions.
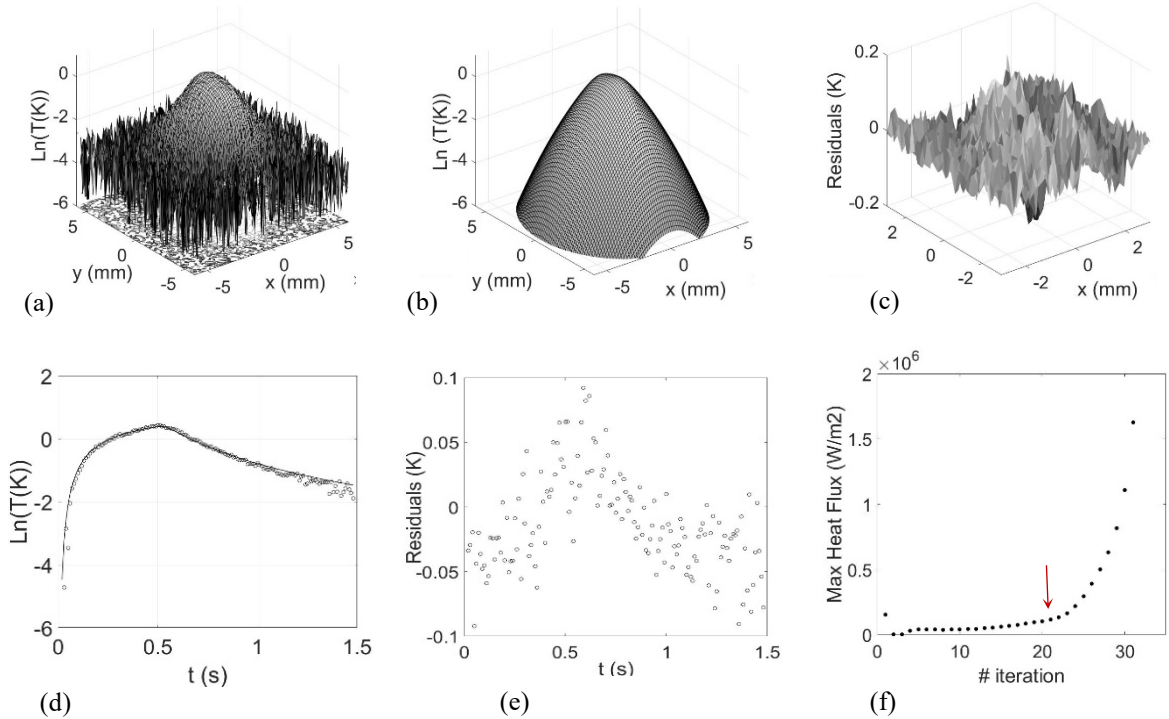

(a) (b) (c)
(d) (e) (f)

Fig. 10 (a) Experimental thermogram obtained at the end of a burst of $\tau = 0.5$ s, for a semi-circular Cu band on radii $r_1 = 1.2$ mm, $r_2 = 2.1$ mm buried at a depth of $d = 0.15$ mm. (b) Fitted thermogram and (c) residuals of the thermogram. (d) Experimental (symbols) and fitted (solid line) timing graph measured at the central pixel, and (e) residuals of the timing graph. (f) Evolution of the maximum flux Q_M along the iteration process. The red arrow indicates the iteration where the process was stopped.

As can be observed in Figure 10, the quality of the fittings is quite good. The residuals in the thermogram (Fig. 10c) are random, and limited to 0.1 K. The residuals in the timing graph

17

(Fig. 10e) are also essentially random and below 0.1 K. The maximum temperature rise in this data set is 1.5 K, so the residuals are below 10%. The 3D representation of the retrieved flux distribution $Q_R(\vec{r})$ and the grey level representation of the normalized heat flux distribution $Q_N(\vec{r})$ retrieved from the inversion are depicted in Figure 11a. In Figs. 11b and 11c we represent the reconstructions obtained for the same Cu slab and longer bursts: 1 and 3.5 s. The maximum flux and total power retrieved from the fittings are also written on each reconstruction.
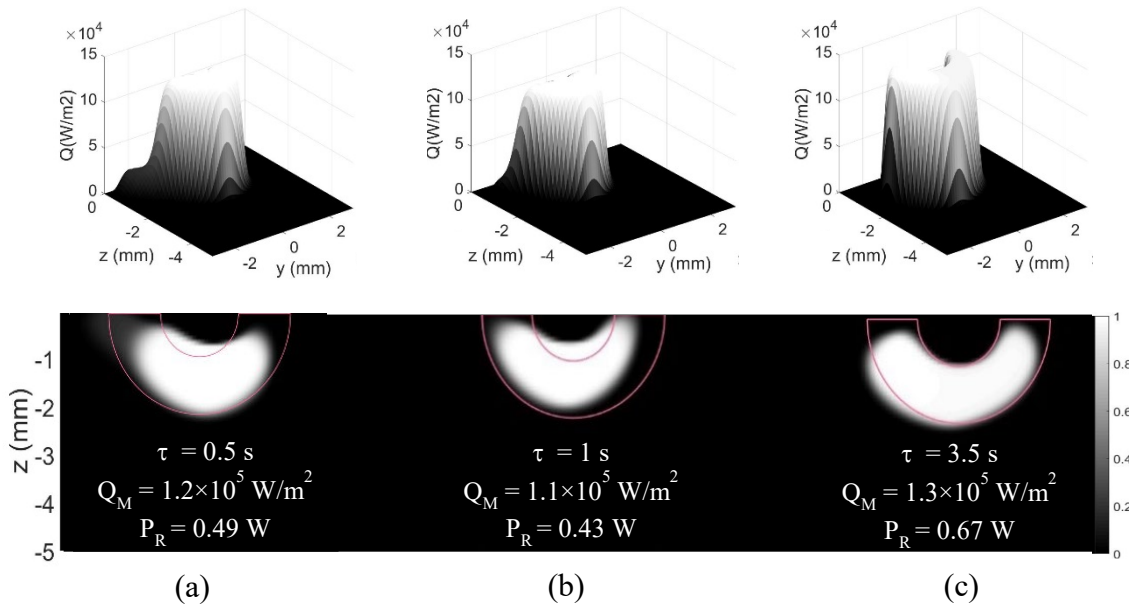

Fig. 11 Top: 3D representations of the heat flux distributions retrieved for a semi-circular Cu band of radii $r_1 = 1.2$ mm, $r_2 = 2.1$ mm buried at a depth of $d = 0.15$ mm, excited with three burst durations: (a) $\tau = 0.5$ s, (b) $\tau = 1$ s, and (c) $\tau = 3.5$ s. Bottom: 2D grey level representation of the normalized heat flux distributions.

The ultrasounds were applied with the same electrical power of 60 W in all cases. Although we do not have reference values for the emitted flux and power, we obtain consistent values of the retrieved maximum flux and total power in the three cases, although the values increase slightly with the (b), (a), (c) sequence. It is worth mentioning that the sequence of data taking was also (b), (a), (c). The increase in the retrieved maximum flux and total power might be associated to variations in the tightening of the screws joining the two steel parts together during the excitation process. These eventual variations in the tightening of the screws may not only affect the total emitted power due to changes in the effective normal force between the Cu

plate and the steel surfaces, but might also lead to symmetry variations of the actual flux distribution caused by uneven tightening of the screws.

We also took data on samples containing Cu slabs of other dimensions and geometries, and buried at different depths. The reconstructions are depicted in Fig. 12, together with the retrieved values of the maximum flux and total power, and the micrographs of the Cu slabs used to take data.
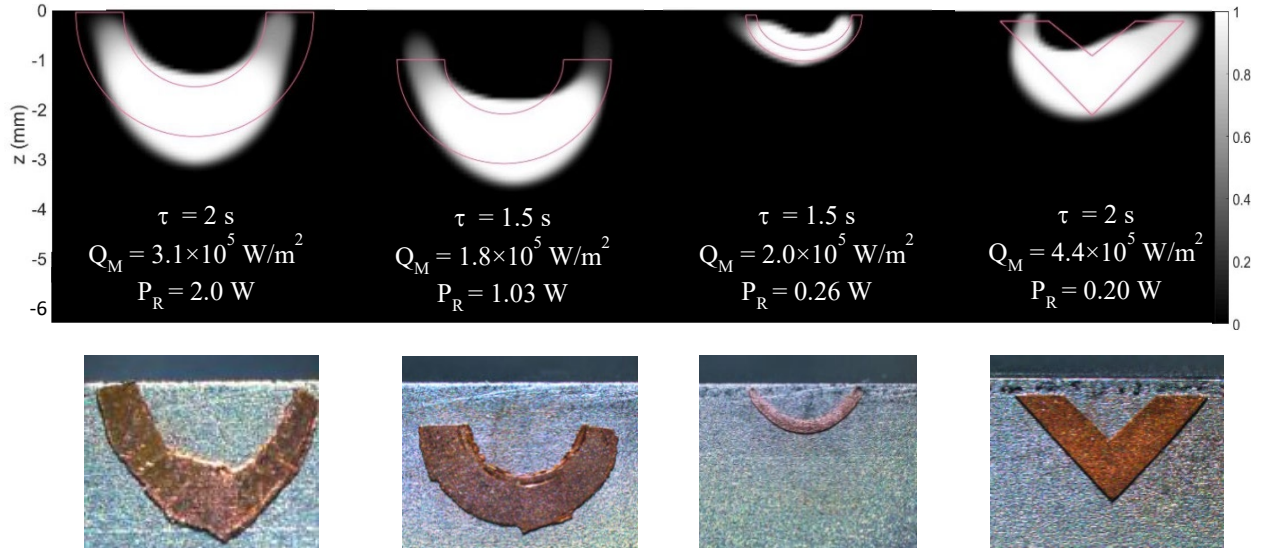

Fig. 12 Top: reconstruction of experimental data obtained with Cu slabs of the geometry indicated by the red line, for different burst durations. The retrieved maximum flux and total power on each reconstruction. Bottom: micrographs of the Cu slabs used to take data.

Finally, we tried to conduct an experiment with an inhomogeneous heat source. Generating a continuously varying and calibrated flux is very challenging in VT experiments. Given that our samples are intended to produce a homogeneous flux over the area of the Cu slab, we decided to use Cu films with different treatments to generate homogeneous (but different) fluxes within both slabs: one of the sheets was made of annealed Cu and the other of hard Cu. We took data on a sample containing two Cu bands with an approximate shape of a quarter of a cycle each made of one type of film (see a micrograph of the Cu slabs on the steel surface in Fig. 13a). In Figs. 13b and 13c we show the 2D grey level representation of the normalized heat flux distribution $Q_N(\vec{r})$ and the 3D representation of the retrieved heat flux distribution $Q_R(\vec{r})$, respectively. As can be seen, the reconstruction exhibits two different areas with almost homogeneous flux, which roughly correspond to the areas of the two Cu slab

quarters. The values of the fluxes retrieved at the two green dots depicted in Fig. 13c with denominations A and B are $Q_A = 1.9 \times 10^5$ W/m^2 and $Q_B = 1.4 \times 10^5$ W/m^2, respectively. The retrieved total emitted power is $P_R = 0.523$ W. Once again, we do not have an independent estimation of the real flux, but the small difference between the fluxes on both sides is plausible, as we obtained the data with two slabs of the same material but slightly different surface condition.
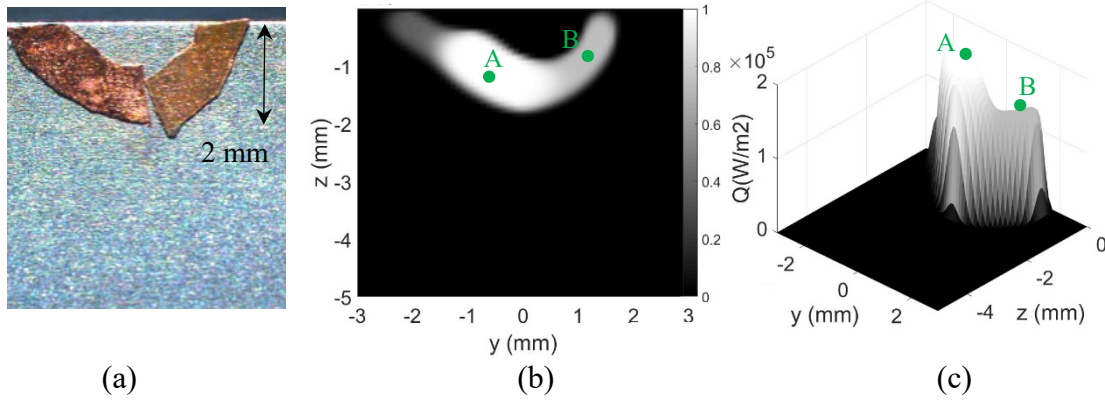

(a) (b) (c)

Fig. 13 (a) Micrograph of the two Cu slabs used to produce an inhomogenous heat flux. (b) 2D grey-level representation of the normalized heat flux distribution $Q_N(\vec{r})$ and (c) 3D representation of the retrieved flux distribution $Q_R(\vec{r})$ for $\tau = 2$ s.

5. Summary and conclusions

We have presented a methodology to characterize the heat flux distribution and the thermal power generated at a vertical open crack in a vibrothermography experiment. The information used is the thermogram obtained at the end of the burst and the evolution of the temperature at the central pixel. Inversions of synthetic data with added uniform noise indicate that the flux distribution is retrieved very accurately in the cases of homogeneous and step-shaped fluxes. Continuously varying fluxes can be characterized if the gradient is not large and occurs preferably in the direction parallel to the surface, but the total emitted power is retrieved very accurately, regardless of the specific spatial dependence. The experiments performed on samples containing geometrically calibrated heat sources provide results that seem consistent, even if there are not references for absolute fluxes and emitted powers. Although the results presented in this work correspond to open cracks, the methodology is also applicable to kissing cracks producing compact heat sources. We believe that this approach, which allows to characterize the flux and power generated at vertical cracks in VT experiments, will be helpful to understand the interrelationship between strain and heat production in VT and may contribute

for further development of the technique. We are currently working on extending the methodology to slanted cracks.

Acknowledgments

References

[1] Henneke EG and Jones TS. Detection of Damage in Composite Materials by vibrothermography, in *Nondestructive Evaluation and Flaw Criticality for Composite Materials* by Amer. Society for Testing and Materials, STP 696, 1979:83-95

[2] Henneke EG, Reifsnider KL and Stinchcomb WW. Thermography - An NDI Method for Damage Detection. J. Met. 1979;31:11-15

[3] Pye J, Adams RD. Detection of damage in fibre reinforced plastics using thermal fields generated during resonant vibration. NDT Int. 1981;14:111-118

[4] Rantala J, Wu D and Busse G. Amplitude-modulated lock-in vibrothermography for NDE of polymers and composites. Res. Nondestr. Eval. 1995;7:215-228

[5] Favro LD, Han X, Ouyang Z, Sun G and Thomas RL. Sonic IR imaging of cracks and delaminations. Analitical Sciences 2001;17:451-453

[6] Mian A, Han X, Islam S and Newaz G. Fatigue damage detection in graphite/epoxy composites using sonic infrared imaging technique. Comp. Sci. Tech. 2004;64:657-666

[7] Barden TJ, Almod DP, Pickering SG, Morbidini M and Cawley P. Detection of impact damage in CFRP composites by thermosonics. Nondestr. Test. Eval. 2007;22:71-82

[8] Fernandes H, Ibarra-Castanedo C, Zhang H and Maldague X. Thermographic nondestructive evaluation of carbon fiber reinforced polymer plates after tensile testing. J. Nondestr. Eval. 2015:34-35:1-10

[9] Favro LD, Han X, Ouyang Z, Sun G and Thomas RL. Sonic IR imaging of cracks and delaminations. Analitical Sciences 2001;17:451-453

[10] Montanini R, Freni F, Rossi GL. Quantitative evaluation of hidden defects in cast iron components using ultrasound activated lock-in vibrothermography. Rev. Sci. Instr. 2012;83:094902 (8pp)

[11] Guo X, Vavilov V. Crack detection in aluminum parts by using ultrasound excited infrared thermography. Infr. Phys. Tech. 2013;61:149-156

[12] Piau JP, Bendada A, Maldague X and Legoux J-G. Nondestructive testing of open microscopic cracks in plasma-sprayed-coatings using ultrasound excited thermography. Nondestr. Test. Eval. 2008;23:109-120

[13] Weekes B, Cawley P, Almond DP, Li T. The effect of crack opening on thermosonics and laser spot thermography. AIP Conf. Proc. 2010;1211:490-497

[14] Lu J, Han X, Newaz G, Favro LD, Thomas RL. Study of the effect of crack closure in sonic infrared imaging. Nondestr. Test. Eval 2007;22:127-135

[15] Renshaw J, Holland SD, Thomson RB. Measurement of crack opening stresses and crack closure stress profiles from heat generation in vibrating cracks. Appl. Phys. Lett. 2008; 93:081914 (3pp)

[16] Renshaw J, Holland SD, Thompson RB, Anderegg J. Vibration induced tribological damage to fracture surfaces via vibrothermography. Int. J. Fatigue 2011;33:849-857

[17] Mendioroz A, Celorrio R, Salazar A. Ultrasound excited thermography: an efficient tool for the characterization of vertical cracks. Meas. Sci. Technol 2017;28:112001(27pp)

[18] Morbidini M, Cawley P. A calibration procedure for sonic infrared nondestructive evaluation. J. Appl. Phys. 2009;106:023504(9pp)

[19] Holland SD, Renshaw J, Roberts R. Measurement of dynamic full-field internal stresses through surface laser Doppler vibrometry. Appl. Phys. Lett. 2007;91:134101(3pp)

[20] Vaddi JS, Holland SD, Kessler MR. Absorptive viscoelastic coatings for full field vibration coverage measurement in vibrothermography. NDT&E Int. 2016;82:56-61

[21] Holland SD, Renshaw J. Physics-based image enhancement for infrared thermography. NDT&E Int. 2010;43:440-445

[22] Mendioroz A, Apiñaniz E, Salazar A, Venegas P, Sáez-Ocáriz I. Quantitative study of buried heat sources by lock-in vibrothermography: an approach to crack characterization. J. Phys. D: Appl. Phys. 2009;42:055502(8pp)

[23] Mendioroz A, Castelo A, Celorrio R, Salazar A. Characterization of vertical buried defects using lock-in vibrothermography: I. Direct problem. Meas. Sci. Technol. 2013;24:065601 (11pp)

[24] Celorrio R, Mendioroz A, Salazar A. Characterization of vertical buried defects using lock-in vibrothermography: II. Inverse problem. Meas. Sci. Technol. 2013;24:065602(9pp)

[25] Mendioroz A, Castelo, A, Celorrio R, Salazar A. Characterization and spatial resolution of cracks using lock-in vibrothermography. NDT&E Int. 2014;66:8-15

[26] Castelo A, Mendioroz A, Celorrio R, Salazar A. Optimizing the inversion protocol to determine the geometry of vertical cracks from lock-in vibrothermography. J. Nondestr. Eval. 2017;36:3(12pp)

[27] Mendioroz A, Celorrio A, Salazar A. Characterization of rectangular vertical cracks using burst vibrothermography. Rev. Sci. Instr. 2015;86:064903(8pp)

[28] Mendioroz A, Celorrio R, Cifuentes A, Zaton L. Salazar A. Sizing vertical cracks using burst vibrothermography, NDT&E Int. 2016;84:36-46

[29] Engl HW, Hanke M, Neubauer A. Regularization of Inverse Problems, Kluwer Academic Publisher, Dordrecht, 2000

[30] Brune C, Sawatzky A, Burger M. Primal and Dual Bregman Methods with Application to Optical Nanoscopy. Int. J. Comput. Vis. 2011;92:211-229

[31] Daubechies I, Defrise M, De Mol C A. An iterative thresholding algorithm for linear inverse problems with a sparsity constraint. Commun. Pure Appl. Math. 2004;11:1413–1457

[32] Bonesky T. Morozov's discrepancy principle and Tikhonov-type functional. Inverse Problems 2009;25:015015-26